J. Fluid Mech. (2017), *vol.* 822, *pp.* 186–201.
doi:10.1017/jfm.2017.278

Spanwise turbulence structure over permeable walls

Kazuhiko Suga[1,†], **Yuka Nakagawa**[1] **and Masayuki Kaneda**[1]

[1]Department of Mechanical Engineering, Osaka Prefecture University, Osaka 599-8531, Japan

(Received 21 January 2017; revised 15 March 2017; accepted 24 April 2017;
first published online 1 June 2017)

Spanwise flow field measurements are carried out for turbulent flows in channels with permeable bottom walls by particle image velocimetry (PIV) to understand the effects of the wall permeability on turbulence structure near porous walls. The porous media used are three kinds of foamed ceramics which have the same porosities (0.8) but different permeabilities. The turbulent flow fields in spanwise planes are discussed using instantaneous and statistical measurement data. At a small permeability Reynolds number (Re_K), low-speed and high-speed streaks, which are similar to those of solid-wall turbulence, are observed near the walls while at a large Re_K the observed structure is very different from that of the solid-wall turbulence. It is found that the obtained spanwise scales of the structure can be reasonably correlated with the wall normal distance plus the zero-plane displacement which is estimated from the mean velocity profile. With the distribution profiles of the spanwise streak spacing and integral length scales, the transitional change of the turbulence structure over permeable walls is discussed.

Key words: turbulent boundary layers, turbulent flows

1. Introduction

Wall surfaces of real materials are usually not perfectly smooth but have roughness and sometimes permeability. Flow characteristics over permeable porous surfaces such as foamed metals, woven or non-woven fabrics and vegetative canopies are different from those over impermeable surfaces. Since it has never been fully understood how different they are, many studies have been performed to discuss flow physics over porous media so far.

The study of Beavers & Joseph (1967) was one of the most classic experimental reports on the friction over porous walls. They reported that the friction factor reduced due to the porosity when the flow was laminar. However, in turbulent flows it turned out to be larger than that over impermeable rough walls (e.g. Lovera & Kennedy 1969; Ruff & Gelhar 1972; Ho & Gelhar 1973; Zagni & Smith 1976). For open channel flows, Zagni & Smith (1976) systematically measured flow rates and velocities over 20 different porous beds made of spherical particles and attributed the increase in the friction factor to additional energy dissipation caused by exchange of momentum across the porous interface. The experiments of Kong & Schetz (1982),

† Email address for correspondence: suga@me.osakafu-u.ac.jp

Zippe & Graf (1983) also indicated that the velocity profiles over the porous layers became more turbulent than those over impermeable rough walls. Using modern particle image velocimetry (PIV), Pokrajac & Manes (2009) measured the detailed flow field over a porous bed composed of glass spheres and concluded that, near the porous interface, turbulent fluctuations of the normal velocity were affected by the permeability.

The above-mentioned experimental reports suggested that the wall permeability affected the flow structure over porous walls, enhancing momentum exchange. Due to the wall permeability, the blocking effect on the wall normal fluctuation velocity is significantly weakened, resulting in stronger near-wall turbulent shear stress. The direct numerical simulation (DNS) studies by Breugem, Boersma & Uittenbogaard (2006), Chandesris *et al.* (2013), Rosti, Cortelezzi & Quadrio (2015) of turbulent porous-walled channel flows also indicated that the effect of the permeability was dominant on turbulence over porous media. To find a turbulence scaling law of flows over permeable walls, systematic studies have been conducted (Breugem *et al.* 2006; Suga *et al.* 2010; Manes, Poggi & Ridol 2011; Suga, Mori & Kaneda 2011). The numerical study by Breugem *et al.* (2006) and the PIV experiments by the present authors' group (Suga *et al.* 2010, 2011; Suga 2016) of turbulent porous-walled channel flows indicated that a permeability Reynolds number was one of the candidates to correlate inner layer phenomena. Suga *et al.* (2010) indicated that the von Kármán coefficient, the zero-plane displacement and the roughness length scale of the semi-logarithmic mean velocity profiles were well correlated with the permeability Reynolds number, defined as $Re_K = u_\tau^p \sqrt{K}/\nu$, with the friction velocity u_τ^p, the wall permeability K and the fluid kinematic viscosity ν. For turbulent boundary layers over polyurethane foam arranged in a laboratory flume, Manes *et al.* (2011) performed laser Doppler anemometer (LDA) measurements. After the discussion on the shear penetration depth and the boundary layer thickness, it was concluded that they could be used respectively for the inner and outer length scales of boundary layers.

Furthermore, due to the wall permeability, the near-wall streaky structure appeared to be destroyed in the DNS studies (Breugem *et al.* 2006; Chandesris *et al.* 2013; Rosti *et al.* 2015; Kuwata & Suga 2016*a*,*b*) of turbulent porous-walled channel flows. Breugem *et al.* (2006) reported that above a highly permeable wall, there were no low- and high-speed streaks and the associated quasi-streamwise vortices. They concluded that turbulent transport across the permeable wall interface prevented the development of elongated streaks. Comparing their simulation results of permeable porous and impermeable rough wall cases, Kuwata & Suga (2016*a*) concluded that over the porous layer, the vortex structure became shredded and the streamwise coherent structure became shorter due to the wall roughness, whereas the pitch of the streaks over the porous layer became approximately twice as wide as that over the impermeable (rough or smooth) walls. Moreover, the presence of the streaks over the porous wall tended to be less visible than those over the impermeable walls.

From the experimental view point, by analysing the PIV data in streamwise-wall-normal (x–y) planes, Suga *et al.* (2011) investigated the near-wall structure and discussed the mechanism behind the destruction of the streaky structure. Their discussions aided by the quadrant analysis confirmed that sweeps became most dominant very near the permeable wall whilst ejections became dominant in the buffer region. Through conditional quadrant-hole analysis of the Reynolds shear stress, it was concluded that due to the increase of the wall permeability, stronger sweeps tended to move towards the wall. However, ejections tended to lose their

strength since the fluid pushed out from the porous wall by the strong inward penetrating motions had already lost its energy inside the porous wall. These effects were generally enhanced by an increase in the permeability Reynolds number. Thus, at least, at a moderate permeability Reynolds number these phenomena resulted in shortening the longitudinal leg vortices of a hairpin vortex since vortex motions could not be maintained with the weakened ejections over highly permeable walls.

However, it is still unknown how the structure of the streaks changes in size and shape due to the wall permeability. Therefore, the present study investigates turbulent vortex structure over permeable walls, focusing on the spanwise flow structure using instantaneous and statistical data by PIV experiments of streamwise–spanwise (x–z) planes. In our previous studies (Suga *et al.* 2010, 2011; Suga 2016), turbulence characteristics were well characterized by the permeability Reynolds number, and there seemed to be a transition to full porous wall turbulence in the range under $Re_K \simeq 3$. Accordingly, the present study attempts to explain the change of the spatial structure when the permeability Reynolds number increases.

2. Experimental method

Figure 1 illustrates the experimental set-up and the coordinate system in the test section of the present study. As shown in figure 1(*a*), tap water is pumped up from a water tank equipped with a cooler (TRL-117GS2, THOMAS KAGAKU) to maintain a constant water temperature of 285±1 K, and its total flow rate is measured by a digital flow meter (FD-MH200A/500A, KEYENCE). The water flow is conditioned by a honeycomb-bundled nozzle, where its temperature is recorded by a digital thermometer (FD-T1, KEYENCE). Then the flow is fully developed in a driver section whose length is 3.0 m and enters the test section of length 1.0 m. Both the sections consist of solid smooth acrylic walls with a porous bottom layer. The sectional width W and total height are, respectively, 0.305 m and 0.093 m, two-thirds of which are filled by a porous layer. For the porous layer, as in the previous reports (Suga *et al.* 2010, 2011; Suga 2016), three kinds of foamed ceramics (shown in figure 2) are used. They are named No. 20, No. 13 and No. 06, and correspond to low-, medium- and high-permeability porous media, respectively. All of them have an isotopic open-cell foam structure with the same porosity of $\varphi = 0.8$, but the mean pore diameter, the permeability and the Forchheimer coefficient vary as $D_p = 1.7$–3.8 mm and $K = 0.020$–0.087 mm^2 and $c_F = 0.17$–0.095, respectively, as listed in table 1. Here, in the measurement of Suga *et al.* (2010) to obtain the permeability and the Forchheimer coefficient, the following Darcy–Forchheimer equation was applied between the pressure drop $\Delta P/\Delta x$ and the Darcy velocity U_d:

$$-\frac{\Delta P}{\Delta x} = \frac{\mu U_d}{K} + \frac{c_F}{K^{1/2}} \rho U_d^2, \tag{2.1}$$

where μ and ρ are the fluid viscosity and density, respectively. Since the height of the clear fluid region is set to $H = 0.03$ m, the aspect ratio of the cross-section of the clear fluid region is approximately 10. To compare the results with those of solid smooth-walled channel flows, a different set of ducts (of height 0.03 m) are also used. By controlling the output of the pump with the power converter, inlet flow rates are adjusted. The measured range of the bulk Reynolds number Re_b ($U_b H/\nu$) is 1500–15 900, where ν is determined by the measured water temperature. To obtain the bulk mean velocity U_b in the clear fluid region, the wall shear stress and the other parameters related to the mean velocity profile, additional corresponding measurements

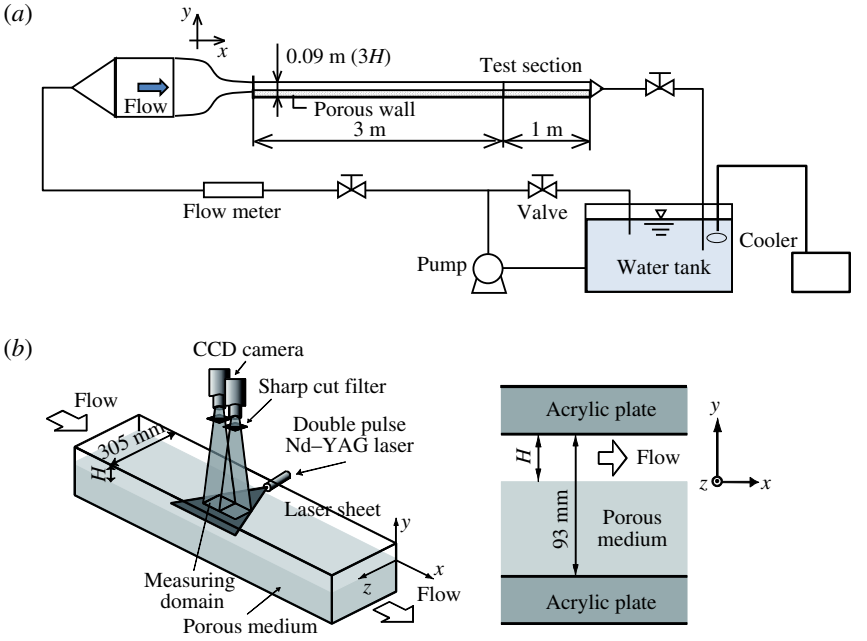

FIGURE 1. (Colour online) Experimental set-up: (*a*) channel flow facility; (*b*) schematic view of the test section.

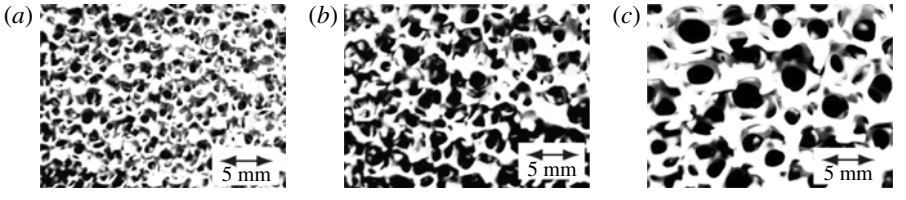

FIGURE 2. Surface photographs of the foamed ceramics: (*a*) No. 20: low permeability, (*b*) No. 13: medium permeability, (*c*) No. 06: high permeability.

Porous med.	φ	D_p (mm)	K (mm^2)	c_F
No. 20	0.82	1.7	0.020	0.17
No. 13	0.81	2.8	0.033	0.10
No. 06	0.80	3.8	0.087	0.095

TABLE 1. Characteristics of the foamed ceramics; φ, D_p, K and c_F are porosity, mean pore diameter, permeability and Forchheimer coefficient, respectively.

of x–y planes at the symmetry of the test section are also performed by the same method as reported in the previous study (Suga *et al.* 2010).

The employed planar PIV system consists of a double-pulse Nd-YAG laser (Dual Power 200-15, Litron) with 200 mJ pulse^{-1} at a wavelength of 532 nm. The laser beam is formed into a sheet approximately 1.0 mm in thickness by several cylindrical lenses and illuminates x–z planes as shown in figure 1(*b*). Two CCD cameras

(Flowsense 4M Mk2, DANTEC DYNAMICS) operating at 30 f.p.s with 85 mm $f/1.8$ lenses (AF Nikkor, Nikon) and extension tubes (Kenko Tokina 12 mm) are arranged in tandem. The recorded frame of each CCD camera covers a zone of $80(x) \times 80(z)$ mm^2 located in the middle of the test section with 2048×2048 pixels, for which 20 % of the area overlaps with another camera's frame.

For the tracer particles, polymer fluorescent particles containing Rhodamine B, whose mean diameter and specific gravity are respectively 10 μm and 1.50, are used. (By Stokes' law, the settling velocity of the particles can be estimated as 2.2×10^{-5} m s^{-1}, which is negligibly small compared with the bulk mean velocity of 6.2×10^{-2} for the lowest Reynolds number case at $Re_b = 1500$.) Correspondingly, a long-pass filter with cutoff wavelength 560 nm is located in front of each camera lens. The seeding density is adjusted to obtain 10–15 particle-image pairs as in Adrian, Meinhart & Tomkins (2000) in each interrogation window of size 32×32 pixels. Thus the measurement sampling volume is $1.25(x) \times 1.0(y) \times 1.25(z)$ mm^3. The image sampling rate is 4 Hz. The timing of the laser pulse interval is adjusted depending on the average particle displacement during the interval. In the present experiments, the average particle displacement is set to be approximately 25 % of the length (3–6 pixels) of the interrogation cell. To obtain the statistical data, in each zone, 4000 image pairs are processed in this study. The recorded data are processed by Dynamics Studio 3.1 (DANTEC DYNAMICS) software with the fast Fourier transform cross-correlation technique (Willert & Gharib 1991). Each image is processed to produce 127×127 vectors from interrogation windows with a 50 % overlap in each direction. When the ratio of the first and the second correlation peaks in an interrogation window is smaller than 1.3, it is removed from the process as an error vector. Furthermore, the moving-average validation (Host-Madsen & McCluskey 1994) is applied with an acceptance factor of 0.1. In the present study, the removed error vectors amount to less than 3 % of the total data processed.

By using image processing software, the average number of pixels for a particle image captured by the CCD camera in the present study is counted to be approximately 3–4 pixels. According to the discussions of Prasad *et al.* (1992), when particle images are well resolved so that the ratio of particle-image diameter to the size of a CCD pixel on the photograph is greater than 3–4, the uncertainty of the measurements is approximately 1/10–1/20 of the particle-image diameter. This indicates that the particle images are well resolved in the present experiments, and the uncertainty in the measured displacement can be expected to be approximately less than 1/10 of the diameter of the particle image. Normalizing this uncertainty by the mean displacement length of particles indicates that the estimated error of the magnitude of the instantaneous velocity is less than 4 % of the maximum velocity near the channel centreline.

3. Results and discussions

Figure 3 shows examples indicating the two-dimensionality of the flow field and the reproducibility of the data between the x–y and x–z plane measurements. From figure 3(*a*), two-dimensionality can be reasonably attained in $z/W = 0.1$–0.9 and the measured flow fields of x–z planes for $z/W = 0.37$–0.63 are well assured to be two-dimensional. It is seen that the measured velocities for the x–z planes agree well with the data of the x–y plane measurement in figure 3(*b*). In the plots of the x–z planes, there is a small gap around $y/H = 0.3$. It suggests that the setting error for the x–z plane measurements was of such an order.

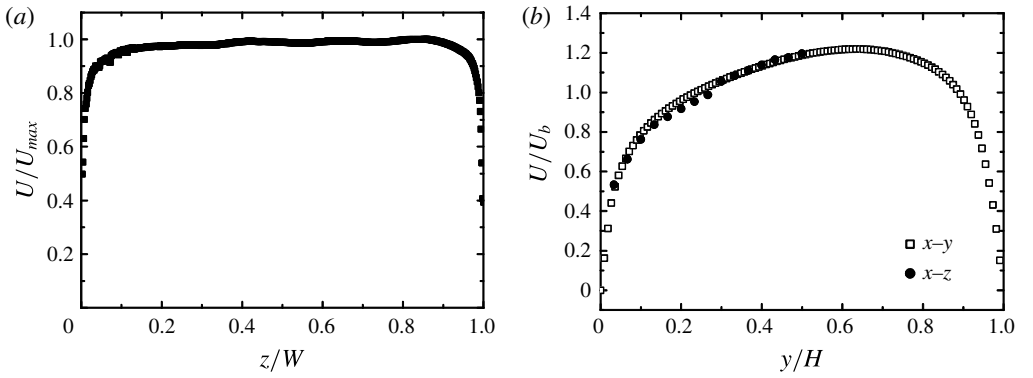

FIGURE 3. Two-dimensionality and reproducibility in the flow field measurements: (*a*) streamwise mean velocity distribution in the spanwise direction at $y/H = 0.5$ and $Re_b = 6200$ for No. 06 porous wall, (*b*) comparison of the streamwise mean velocity distribution between *x*–*y* and *x*–*z* plane measurements at $Re_b = 3100$ for No. 13 porous wall.

The *x*–*z* plane measurements are performed for solid smooth wall, No. 20, No. 13 and No. 06 porous wall cases, changing Re_b from 1500 to 15 900 to achieve the conditions of Re_K approximately at 1.0, 2.0, 3.0, 6.0 and 10.0. There are altogether 15 cases, as shown in table 2. For each case, several measurement planes in the wall normal direction are measured. In table 2, measured sections 5, 5*, 14, 14*, 15 and 18 correspond to sections of (1.0, 2.0, 3.0, 4.0, 5.0 mm), (0.5, 1.0, 1.5, 2.0, 2.5 mm), (1.0, 2.0, 3.0, . . . , 14.0, 15.0 mm), (1.0, 2.0, 3.0, . . . , 13.0, 14.0 mm), (0.5, 1.0, 1.5, 2.0, 2.5, 3.0, 4.0, . . . , 10.0, 11.0 mm) and (0.5, 1.0, 1.5, 2.0, 2.5, 3.0, 4.0, . . . , 14.0, 15.0 mm) from the bottom surface, respectively.

3.1. *Snapshots of streaks*

Figure 4 shows snapshots of the instantaneous streamwise velocity fluctuation u' indicating low- and high-speed streaks and corresponding vorticity maps over porous walls at $y^{p+} \simeq 20$, where $(\cdot)^{p+}$ is a value normalized by the friction velocity u_τ^p on the porous wall which is estimated by extrapolating the Reynolds shear stress distribution obtained by the corresponding *x*–*y* plane measurement. Since in the previous study (Suga *et al.* 2010) all the data for No. 20, No. 13 and No. 06 porous media were well correlated with Re_K, figure 4 arranges the snapshots in the order of Re_K irrespective of the porous media. (Indeed, the patterns of different porous medium cases are very similar to each other at similar Re_K conditions.) Note that $y = 0$ corresponds to the porous wall surface and all area sizes of the sub-figures are set to $L_x^{p+} \times L_z^{p+} = 990 \times 550$ to compare the scales of structural elements. The existence of the streaky structure is obvious in figure 4(*a*–*d*) at $Re_K = 0.93$–1.79 although they are twisted. It is obvious that the patterns in the vorticity ω_y^{p+} maps are consistent with those in the maps of the high- and low-speed streaks. In figure 4(*e*,*f*) at $Re_K = 2.94$, the twisting degree significantly increases and the streaks tend to be torn into fragments. Such a tendency is obvious in the vorticity map of figure 4(*f*), and longitudinally elongated streaks can no longer be observed. Accordingly, it is confirmed that the quasi-streak-like structure is maintained near a wall at a lower Re_K, while it tends to be destroyed as Re_K increases.

At the higher-Re_K cases of $Re_K = 6.23$ and 11.12, in figure 4(*g*–*j*), although low- and high-speed fluid lumps exist, obvious streak-like vorticity patterns cannot be

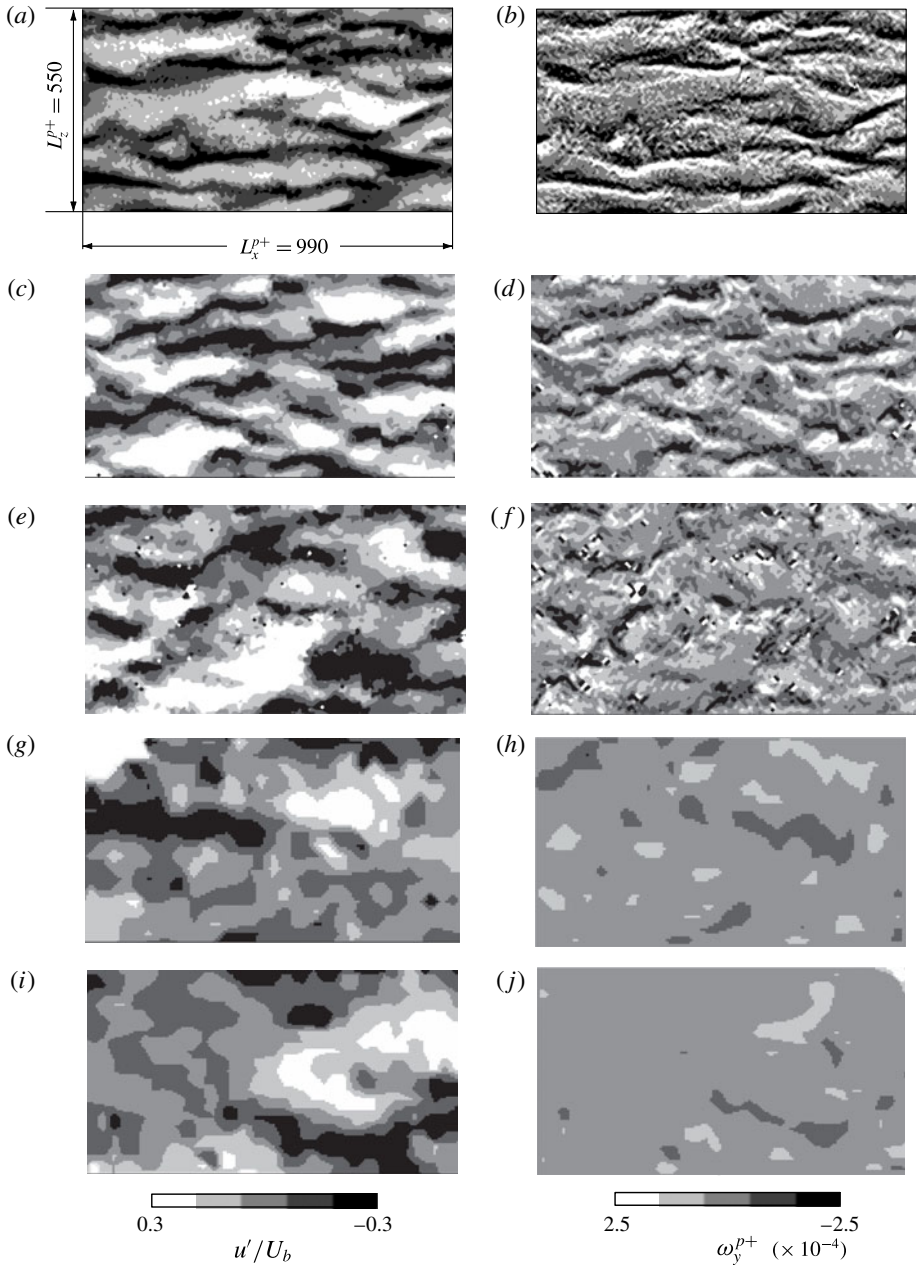

FIGURE 4. Snapshots of streamwise velocity fluctuation indicating low- and high-speed streaks and instantaneous wall normal vorticity $\omega_y^{p+} = (\partial u/\partial z - \partial w/\partial x)\nu/(u_\tau^{p+})^2$ in the window of $L_x^{p+} \times L_z^{p+} = 990 \times 550$ at $y^{p+} \simeq 20$: (*a*,*c*,*e*,*g*,*i*) are fluctuation velocity contours and (*b*,*d*,*f*,*h*,*j*) are vorticity contours. (*a*,*b*) No. 20 porous wall at $Re_K = 0.93$ and $Re_b = 2500$, (*c*,*d*) No. 13 porous wall at $Re_K = 1.79$ and $Re_b = 3100$, (*e*,*f*) No. 06 porous wall at $Re_K = 2.94$ and $Re_b = 2700$, (*g*,*h*) No. 20 porous wall at $Re_K = 6.23$ and $Re_b = 14800$, (*i*,*j*) No. 06 porous wall at $Re_K = 11.12$ and $Re_b = 9900$. The flow direction is left to right.

Bottom wall	Meas. sec.	Re_b	Re_K	u_τ^p/u_τ^t	κ	d^{p+}	h^{p+}
Solid	5	5 600	—	1.00	—	—	—
No. 20	5	2 500	0.93	1.14	0.40	0	0
	18	5 200	1.90	1.23	0.37	7	1
	14*	7 200	2.90	1.34	0.29	38	6
	5*	14 800	6.23	1.46	0.28	56	17
No. 13	5	1 900	1.07	1.22	—	—	—
	15	3 100	1.79	1.34	0.33	11	2
	14	4 700	3.00	1.43	0.27	45	12
	5*	10 800	6.45	1.54	0.25	76	28
	5*	15 900	9.35	1.57	0.28	94	31
No. 06	15	1 500	1.80	1.36	—	—	—
	5*	2 700	2.94	1.45	0.32	21	5
	5	3 400	3.83	1.52	0.28	26	9
	15	6 200	6.73	1.63	0.26	80	27
	5*	9 900	11.12	1.70	0.28	123	41

TABLE 2. Experimental conditions and measured parameters of the mean velocity fields; u_τ^t and u_τ^p are the friction velocities on the top solid and bottom porous walls; κ, d and h are the von Kármán coefficient, the zero-plane displacement and the roughness length scale, respectively; $(\cdot)^{p+}$ corresponds to a value normalized by using u_τ^p.

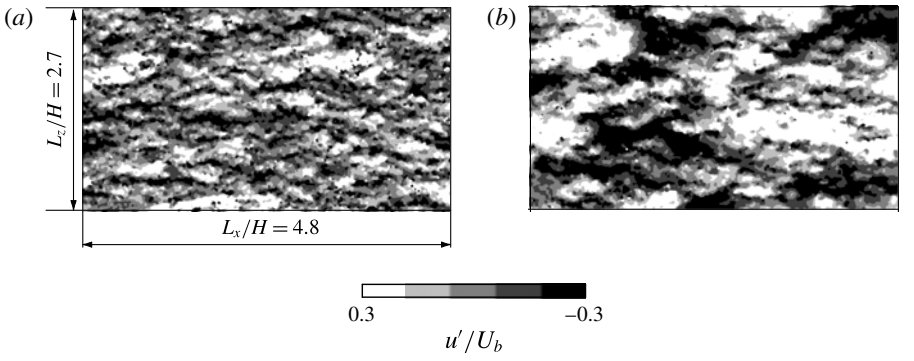

FIGURE 5. Snapshots of low- and high-speed fluid lumps in the measurement areas of $L_x/H \times L_z/H = 4.8 \times 2.7$ at $y^{p+} \simeq 20$: (*a*) No. 20 porous wall at $Re_K = 6.23$ and $Re_b = 14800$ (corresponding to figure 4*g*), (*b*) No. 06 porous wall at $Re_K = 11.12$ and $Re_b = 9900$ (corresponding to figure 4*i*).

observed in the windows of $L_x^{p+} \times L_z^{p+} = 990 \times 550$. To see those fluid lumps on a wider scale, figure 5 shows patterns of low- and high-speed fluid lumps for the cases of figure 4(*g*,*i*). The window size of these sub-figures is $L_x/H \times L_z/H = 4.8 \times 2.7$, which corresponds to $L_x^{p+} \times L_z^{p+} = 6670 \times 3670$ and 5660×3100 for figures 5(*a*) and 5(*b*), respectively. Obviously, the pattens shown in figure 5 are very different from the longitudinally elongated streak structure, and large-scale spanwise patterns seem to be developing as in figure 5(*b*). Indeed, in the streamwise direction, black and white block areas can be seen in turn. This is considered to be footprints of

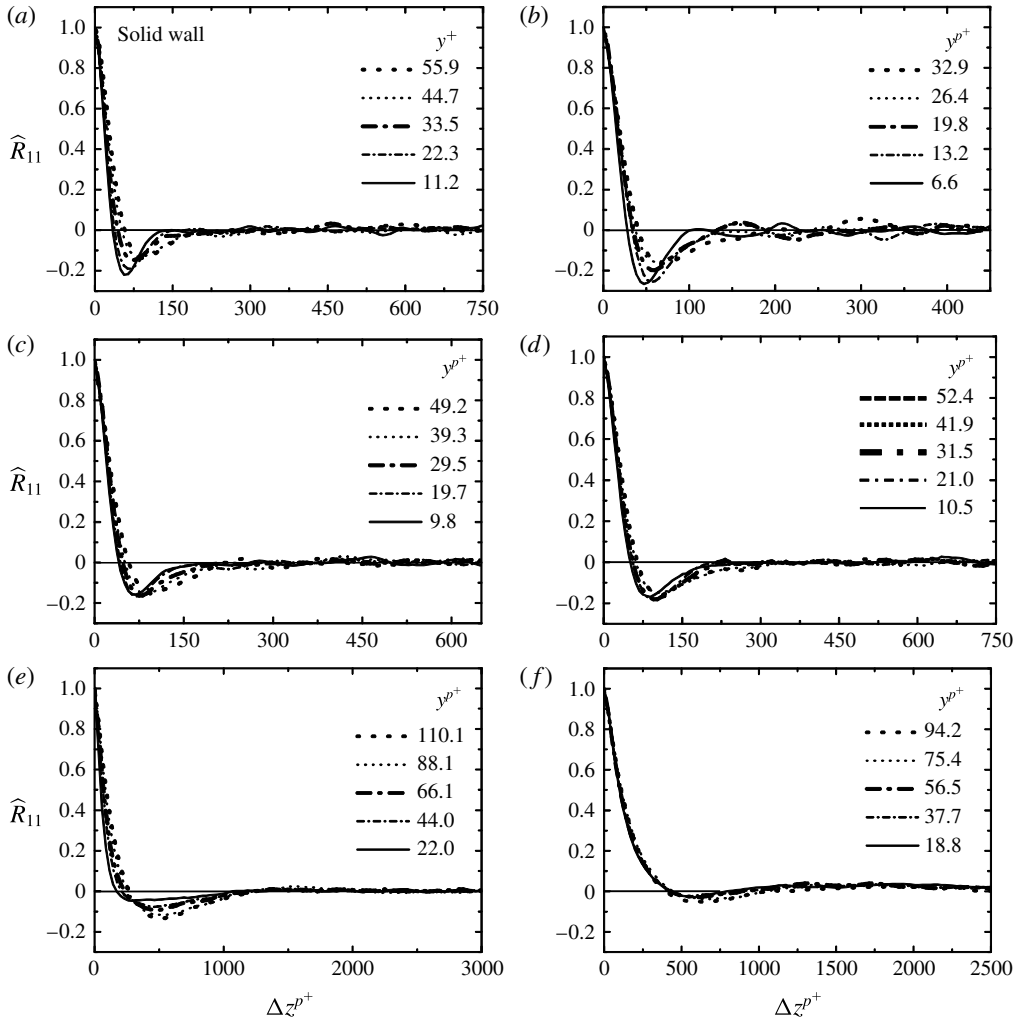

FIGURE 6. Two-point correlation of the streamwise velocity versus spanwise spacing: (*a*) solid wall at $Re_b = 5600$, (*b*) porous wall No. 20 at $Re_K = 0.93$ and $Re_b = 2500$, (*c*) porous wall No. 13 at $Re_K = 1.79$ and $Re_b = 3100$, (*d*) porous wall No. 06 at $Re_K = 2.94$ and $Re_b = 2700$, (*e*) porous wall No. 20 at $Re_K = 6.23$ and $Re_b = 14\,800$, (*f*) porous wall No. 06 at $Re_K = 11.12$ and $Re_b = 9900$.

the spanwise transverse rolls induced by the Kelvin–Helmholtz (K–H) instability as reported numerically by Jiménez *et al.* (2001) and Kuwata & Suga (2016*a*).

3.2. *Scales of spanwise structure*

To discuss scales of the coherent structure, the normalized two-point correlation function:

$$\widehat{R_{ij}}(\Delta z) = R_{ij}(\Delta z)/R_{ij}(0) = \overline{u_i'(z)u_j'(z+\Delta z)}/\overline{u_i'(z)u_j'(z)}, \tag{3.1}$$

in the spanwise direction is discussed. Figure 6 shows $\widehat{R_{11}}(\Delta z)$ distributions which correspond to the solid-wall case: figure 6(*a*), and the five Re_K cases shown in figure 4.

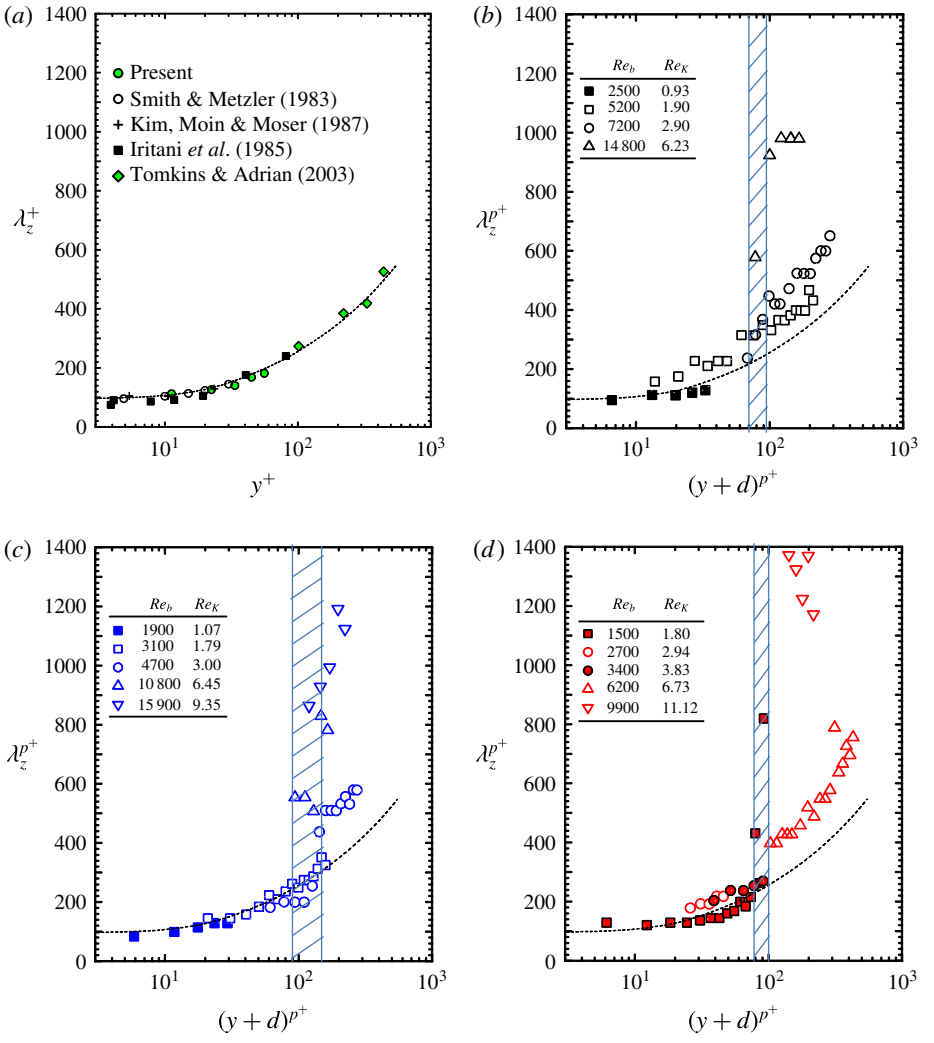

FIGURE 7. (Colour online) Distribution of spanwise spacing of streaks in the wall normal direction: (*a*) solid wall, (*b*) porous wall No. 20, (*c*) porous wall No. 13, (*d*) porous wall No. 06; hatching zone is the zone where the plots start to deviate largely from the broken line; broken line indicates the fitting line of the solid-wall cases.

For all the cases local minima can be seen, while their depths (magnitudes) and positions change depending on the wall normal distance. This trend is consistent with the results of Breugem *et al.* (2006). Moreover, generally the depth tends to decrease, and the oscillations observed after the local minima vanish as Re_K increases. Since the local minimum corresponds to the average spanwise distance between low-speed and neighbouring high-speed regions, the decrease of its magnitude and vanishing oscillations indicate that the streak structure tends to vanish as Re_K increases.

From the locations of the local minima, the distributions of the spanwise spacing of streaks λ_z^{p+} (or λ_z^+ for solid walls) against the wall normal distance (plus the zero-plane displacement) are obtained as in figure 7. Figure 7(*a*) compares the solid smooth wall results and published data in the literature (Smith & Metzler 1983; Iritani, Kasagi

& Hirata 1985; Kim, Moin & Moser 1987; Tomkins & Adrian 2003). It is seen that all the data align well on a single curve, indicating that the streaks over the solid smooth walls are well organized and their spacing is approximately 100 wall units under $y^+ = 20$, while it gradually increases as the wall normal distance increases.

In figure 7(*b–d*), it is found that the points of λ_z^{p+} collapse around the curve under $(y+d)^{p+} \simeq 100$ reasonably well when the zero-plane displacement d is combined with the wall normal distance. The zero-plane displacement is a parameter in the log-law form for the mean velocity over porous walls. (See appendix A for comments on the parameters of log-law velocities listed in table 2.) Indeed, in figure 7(*b–d*) plots for No. 20, No. 13 and No. 06 cases are in reasonable agreement with the line representing the correlation of the solid-wall case under $(y+d)^{p+} \simeq 70$, 90 and 80, respectively. It is considered that quasi-coherent streaks over a porous wall generated by the wall shear are pushed into the porous wall by downward motions of the K–H waves. Since the zero-plane displacement is considered to be a length scale associated with the penetration, the agreement between the plots and lines in figure 7(*b–d*) suggests that the structure retains the characteristics of streaks even if their bottom parts penetrate into the porous walls. Hence, λ_z^{p+} shows the correlation with $(y+d)^{p+}$. However, at positions of certain distances from the wall surfaces, in the regions which are marked by hatching zones, the plotted values start to deviate largely from the correlation line. Although the ranges of the hatching zones are different in the porous layer cases, their locations are around $(y+d)^{p+} \simeq 100$. This region where the trend changes is considered to be a structural transition region. It is considered that the quasi-streaky structure is smeared or may no longer exist over such regions. Indeed, the snapshots shown in figure 5 are the cases inside and over the hatching zones.

Suga *et al.* (2011) observed another transitional change in the distributions of turbulence fluctuation velocities over porous walls. The shape of the joint probability density function $p(u', v')$ of the fluctuation velocity at $y^{p+} \simeq 15$ changed in the condition under $Re_K \simeq 3$. (The turbulence anisotropy tended to rapidly weaken as Re_K increased up to $Re_K \simeq 3$.) The location at $y^{p+} \simeq 15$ under $Re_K \simeq 3$ corresponds to the region under $(y+d)^{p+} \simeq 47$ if the correlation $d^{p+} \simeq 15.1 Re_K - 13.5$, which was seen in Suga *et al.* (2010), is valid. (In the present cases of $Re_K = 2.90$–3.00, $y^{p+} = 15$ corresponds to $(y+d)^{p+} = 36 - 60$.) This indicates that the transitional change of the spanwise turbulence scale occurs after the transitional change of the near-wall turbulence anisotropy.

To see the vortex length scales, figure 8 shows the distribution of the spanwise integral length Λ_{11}, which is defined as

$$\Lambda_{ij} = \frac{1}{2\overline{u_i'(z)u_j'(z)}} \int_{-\infty}^{\infty} R_{ij}(r)\,\mathrm{d}r. \tag{3.2}$$

It is seen that a cluster involving the solid-wall case extends up to $(y+d)^{p+} \simeq 300$ and the length scale size ranges as $\Lambda_{11}^{p+} = 5$–25. However, it is indicated that at $(y+d)^{p+} > 100$, flow motions with much larger scales coexist and start to be dominant. This suggests that fragments of the torn longitudinal vortex tubes are entrained by the large-scale fluid lumps moving with travelling transverse waves.

4. Concluding summary

At a lower Re_K, low- and high-speed streaks, which are similar to those of solid-wall turbulence, are observed near the permeable walls. In case of a large

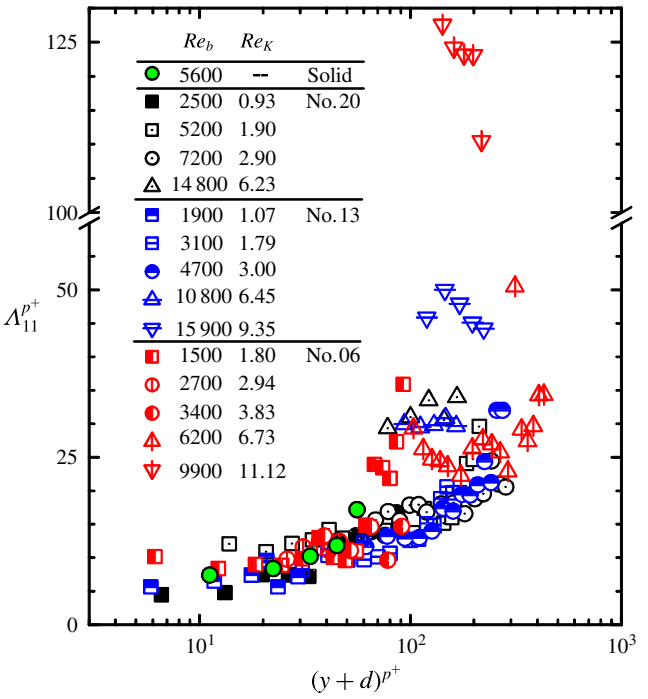

FIGURE 8. (Colour online) Integral length variations in the wall normal direction.

Re_K, although some large-scale patterns are observed in the velocity field, they are confirmed to be very different from those of the solid-wall turbulence structure. It is found that the spanwise spacing of the streaks λ_z and the spanwise integral length Λ_{11} can be reasonably correlated with the wall normal distance including the zero-plane displacement d of the log-law mean velocity profile. Since there is a correlation between d^{p+} and Re_K (Suga *et al.* 2010), these phenomena have a correlation with Re_K via d^{p+}. It is considered that quasi-coherent streaks over permeable walls generated by the wall shear are pushed into the porous walls by the downward motions of the K–H waves. Since the zero-plane displacement d is considered to be a length scale associated with the penetration, the distribution profiles of those scales (λ_z and Λ_{11}) indicate that the structure keeps the characteristics of streaks even if their bottom parts penetrate into the porous walls. Accordingly, the surviving elements of the streaks exist and their scales maintain correlations with the wall normal distance under the transitional range starting from $(y+d)^{p+} \simeq 100$, while those elements tend to be disturbed by the K–H instability as the wall normal distance increases. From the region at $(y+d)^{p+} > 100$, flow motions with much larger spanwise length scales start to be dominant. Such flow motions are considered to be transverse roll cells which are generated by the K–H instability and destroy the longitudinal vortex trails. It is considered that fragments of the torn longitudinal vortex tubes surf over the transverse travelling waves. When Re_K is large enough, d^{p+} becomes close to or even surpasses 100, resulting in the loss of the quasi-streak structure near the surfaces.

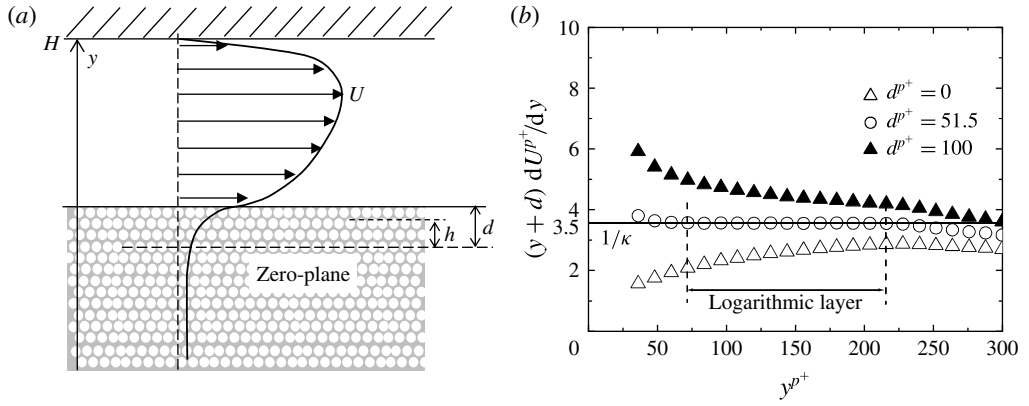

FIGURE 9. Parameters of mean velocity: (*a*) zero-plane displacement d and roughness length scale h, (*b*) logarithmic layer indicated by $(y+d)\,\mathrm{d}U^{p+}/\mathrm{d}y$.

Acknowledgements

The authors thank their colleague A. Taneo for processing the experimental data. A part of this study was financially supported by a research grant (no. 24360073) of the JSPS Japan.

Appendix A. Parameters of log-law velocity profile

For turbulent flows above rough beds or submerged canopies, following Best (1935), the log-law form:

$$U^+ = \frac{1}{\kappa}\ln\left(\frac{y+d}{h}\right), \tag{A 1}$$

is usually applied (e.g. Nikora *et al.* 2002; Nepf & Ghisalberti 2008; Suga *et al.* 2010; Manes *et al.* 2011), where κ is the von Kármán coefficient, h is the roughness length scale and d is the depth of the zero-plane from the surface in the present geometrical definition. Figure 9(*a*) illustrates those parameters. Note that the correlation by Nikuradse (1933) for rough wall boundary layers is essentially the same as (A 1) if the origin of y-axis is set to the zero-plane illustrated in figure 9(*a*). Table 2 lists the values of κ, d and h obtained by the fitting method for velocity profiles described below. (At $Re_b < 2000$, the values are not listed in table 2 since the logarithmic layers cannot be obviously recognized.) Although the listed values of d and h are non-dimensionalized, they can be easily dimensionalized by taking ratios by Re_K. For example, since $d^{p+}/Re_K = (u_\tau^p d/\nu)/(u_\tau^p K^{1/2}/\nu) = d/K^{1/2}$, with the value of the permeability listed in table 1 one can calculate the dimensional value of d.

The extent of the logarithmic layer can be determined from plots of $(y+d)\,\mathrm{d}U^+/\mathrm{d}y$ as a function of y^+, changing the values of d (Breugem *et al.* 2006). Since $(y+d)\,\mathrm{d}U^+/\mathrm{d}y$ must be a constant equal to $1/\kappa$ inside the logarithmic layer, a value of d giving a flat plateau in the profile must be the best fitted value. For example, in figure 9(*b*), a flat plateau can be obtained with $d^{p+} = 51.5$ and the value of the plateau becomes $(y+d)\,\mathrm{d}U^+/\mathrm{d}y = 3.5$, which corresponds to $1/\kappa$ to be obtained. Then, with these d and κ, equation (A 1) is best fitted to the velocity profile to obtain the roughness length scale h.

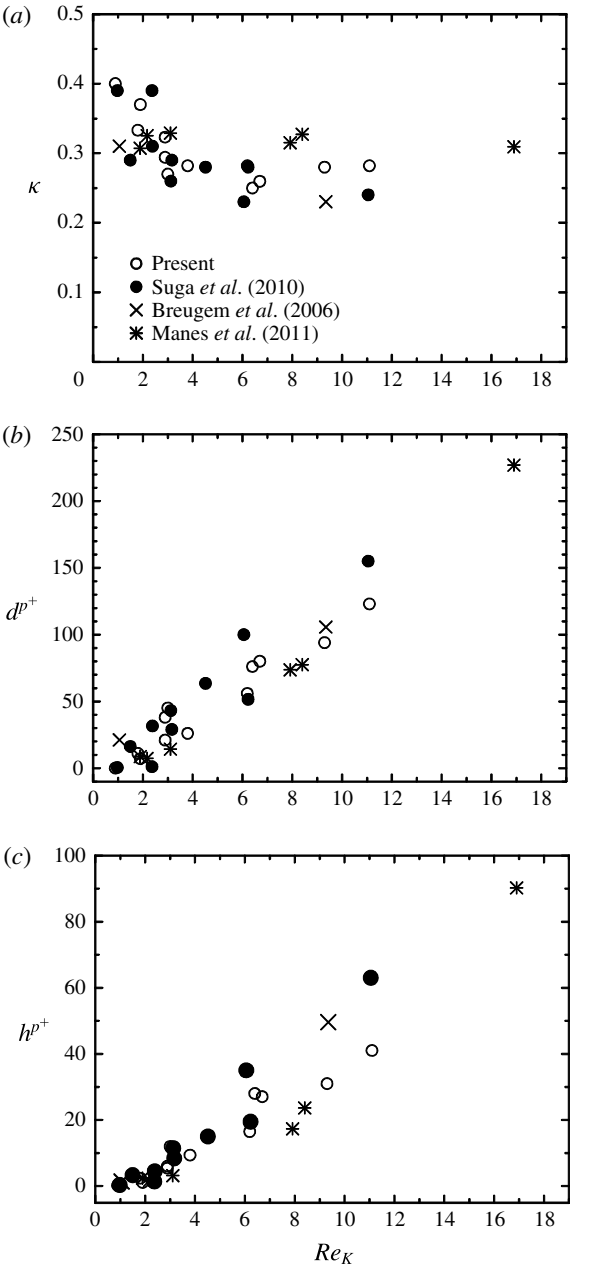

FIGURE 10. Distribution of parameters of mean velocity profiles against the permeability Reynolds number: (*a*) von Kármán coefficient, (*b*) zero-plane displacement, (*c*) roughness length scale; ○, ●, × and ∗ are the present data, the data of Suga *et al.* (2010), Breugem *et al.* (2006) and Manes *et al.* (2011), respectively.

Suga *et al.* (2010) found that κ, d^{p+} and h^{p+} had close relationships with the permeability Reynolds number. As seen in figure 10, the data of Suga *et al.* (2010) and the present study suggest relationships between Re_K and the parameters.

It is noticeable that, as Re_K increases, κ becomes smaller than 0.4 while generally d^{p+} and h^{p+} monotonically increase. Breugem *et al.* (2006) also reported that κ decreased to 0.23 and 0.31, respectively, in the cases of $\varphi = 0.95$ and 0.8 of turbulent porous-walled channel flows at $Re_b = 5500$. Their permeability Reynolds numbers correspond to $Re_K = 1.06$ and 9.35, respectively. In the turbulent open channel flows over polyurethane foam beds whose porosities were 96.4−98.0 by Manes *et al.* (2011), κ ranged between 0.31 and 0.33, depending on the permeability Reynolds number at $Re_K = 1.9$–17.2. Those results shown in figure 10(*a*) support that κ becomes smaller than 0.4 in flows over highly porous walls. Such low values of κ are mainly related to the wall permeability, as Breugem *et al.* (2006) concluded, since κ is usually approximately 0.4 even for rough walls as in Raupach, Antonia & Rajagopalan (1991). The data points in figure 10(*a*) indicate that there is a relationship between κ and Re_K, though with a certain amount of scattering. As seen in figure 10(*b*,*c*), d^{p+} and h^{p+} increase as Re_K increases. These trends are also consistent with the results of Breugem *et al.* (2006) and Manes *et al.* (2011).

REFERENCES

ADRIAN, R. J., MEINHART, C. D. & TOMKINS, C. D. 2000 Vortex organization in the outer region of the turbulent boundary layer. *J. Fluid Mech.* **422**, 1–54.

BEAVERS, G. S. & JOSEPH, D. D. 1967 Boundary conditions at a naturally permeable wall. *J. Fluid Mech.* **30**, 197–207.

BEST, A. C. 1935 Transfer of heat and momentum in lowest layers of the atmosphere. *Tech. Rep.* 65. Geophys. Mem., Met. Off. Lond.

BREUGEM, W. P., BOERSMA, B. J. & UITTENBOGAARD, R. E. 2006 The influence of wall permeability on turbulent channel flow. *J. Fluid Mech.* **562**, 35–72.

CHANDESRIS, M., D'HUEPPE, A., MATHIEU, B., JAMET, D. & GOYEAU, B. 2013 Direct numerical simulation of turbulent heat transfer in a fluid-porous domain. *Phys. Fluids* **25** (12), 125110.

HO, R. T. & GELHAR, L. W. 1973 Turbulent flow with wavy permeable boundaries. *J. Fluid Mech.* **58**, 403–414.

HOST-MADSEN, A. & MCCLUSKEY, D. R. 1994 On the accuracy and reliability of PIV measurements. In *7th International Symposium Application of Laser Techniques to Fluid Mechanics, Lisboa, Portugal*, pp. 214–226.

IRITANI, Y., KASAGI, N. & HIRATA, M. 1985 Heat transfer mechanism and associated turbulence structure in the near-wall region of a turbulent boundary layer. *Turb. Shear Flows* **4**, 2223–2234.

JIMÉNEZ, J., UHLMANN, M., PINELLI, A. & KAWAHARA, G. 2001 Turbulent shear flow over active and passive porous surfaces. *J. Fluid Mech.* **442**, 89–117.

KIM, J., MOIN, P. & MOSER, R. 1987 Turbulence statistics in fully developed channel flow at low Reynolds number. *J. Fluid Mech.* **177**, 133–166.

KONG, F. Y. & SCHETZ, J. A. 1982 Turbulent boundary layer over porous surfaces with different surface geometries. *AIAA Paper* 82-0030.

KUWATA, Y. & SUGA, K. 2016*a* Lattice Boltzmann direct numerical simulation of interface turbulence over porous and rough walls. *Intl J. Heat Fluid Flow* **61**, 145–157.

KUWATA, Y. & SUGA, K. 2016*b* Transport mechanism of interface turbulence over porous and rough walls. *Flow Turbul. Combust.* **97**, 1071–1093.

LOVERA, F. & KENNEDY, J. F. 1969 Friction factors for flat bed flows in sand channels. *J. Hydraul. Div. ASCE* **95**, 1227–1234.

MANES, C., POGGI, D. & RIDOL, L. 2011 Turbulent boundary layers over permeable walls: scaling and near-wall structure. *J. Fluid Mech.* **687**, 141–170.

NEPF, H. & GHISALBERTI, M. 2008 Flow and transport in channels with submerged vegetation. *Acta Geophys.* **56**, 753–777.

NIKORA, V., KOLL, K., MCLEAN, S., DITTRICH, A. & ABERLE, J. 2002 Zero-plane displacement for rough-bed open-channel flows. In *International Conference on Fluvial Hydraulics River Flow 2002, Louvain-la-Neuve, Belgium*, pp. 83–92. Swets & Zeitlinger, Lisse, The Netherland.

NIKURADSE, J. 1933 Strömungsgesetze in rauhen Rohren. *VDI-Forschungsheft* 361.

POKRAJAC, D. & MANES, C. 2009 Velocity measurements of a free-surface turbulent flow penetrating a porous medium composed of uniform-size spheres. *Transp. Porous Med.* **78**, 367–383.

PRASAD, A. K., ADRIAN, R. J., LANDRETH, C. C. & OFFUTT, P. W. 1992 Effect of resolution on the speed and accuracy of particle image velocimetry interrogation. *Exp. Fluids* **13**, 105–116.

RAUPACH, M. R., ANTONIA, R. A. & RAJAGOPALAN, S. 1991 Rough-wall turbulent boundary layers. *Appl. Mech. Rev.* **44**, 1–25.

ROSTI, M. E., CORTELEZZI, L. & QUADRIO, M. 2015 Direct numerical simulation of turbulent channel flow over porous walls. *J. Fluid Mech.* **784**, 396–442.

RUFF, J. F. & GELHAR, L. W. 1972 Turbulent shear flow in porous boundary. *J. Engng Mech. ASCE* **98**, 975–991.

SMITH, C. R. & METZLER, S. P. 1983 The characteristics of low-speed streaks in the near-wall region of a turbulent boundary layer. *J. Fluid Mech.* **129**, 27–54.

SUGA, K. 2016 Understanding and modelling turbulence over and inside porous media. *Flow Turb. Combust.* **96**, 717–756.

SUGA, K., MATSUMURA, Y., ASHITAKA, Y., TOMINAGA, S. & KANEDA, M. 2010 Effects of wall permeability on turbulence. *Intl J. Heat Fluid Flow* **31**, 974–984.

SUGA, K., MORI, M. & KANEDA, M. 2011 Vortex structure of turbulence over permeable walls. *Intl J. Heat Fluid Flow* **32**, 586–595.

TOMKINS, C. D. & ADRIAN, R. J. 2003 Spanwise structure and scale growth in turbulent boundary layers. *J. Fluid Mech.* **490**, 37–74.

WILLERT, C. E. & GHARIB, M. 1991 Digital particle image velocimetry. *Exp. Fluids* **10**, 181–193.

ZAGNI, A. F. E. & SMITH, K. V. H. 1976 Channel flow over permeable beds of graded spheres. *J. Hydraul. Div.* **102**, 207–222.

ZIPPE, H. J. & GRAF, W. H. 1983 Turbulent boundary-layer flow over permeable and non-permeable rough surfaces. *J. Hydraul. Res.* **21**, 51–65.